Galvanic replacement-induced introduction of a heteroligand into bimetallic and trimetallic nanoclusters

Jian-Hong Liao, Tzu-Hao Chiu, Hao Liang, Samia Kahlal, Jean-Yves Saillard, C.W. Liu

Galvanic-Replacement-Induced Introduction of an Hetero-ligand into Bimetallic and Trimetallic Nanoclusters†

Jian-Hong Liao,[a] Tzu-Hao Chiu,[a] Hao Liang,[b] Samia Kahlal,[b] Jean-Yves Saillard *[b] and C. W. Liu *[a]

Heteroleptic eight-electron silver-rich alloy nanoclusters, $[Au@Au_4Ag_{12}(dtp)_7(PPh_3)_4]^{2+}$ (1), and $[Pt@Au_4Ag_{11}(dtp)_7(PPh_3)_4]$ (2) were successfully synthesized via galvanic-replacement reaction of 1,1-dithiolate-protected $M@Ag_{20}$ (M = Au, Pt) nanoclusters with Au(I)-phosphine salts leading to the alteration of the cluster nuclearity and geometry of shell skeletons but retaining the same 8-electron count.

Ligand-protected metal nanoclusters (NCs) with atom-precise compositions have undergone many developments in their fine-tuning optical, catalytic, and biomedical applications.[1-3] These NCs exhibit optical properties that are correlated to several factors, such as the geometry and electron count of their kernel, the presence of a dopant (if any), the nature of the ligand-protected layer, and the possible supramolecular assembly of the NCs.[4-10] Thus, molecular engineering on these features has become a fascinating task. A commonly used method for alloying homo-metallic NCs is to introduce hetero-metals into their framework via galvanic or anti-galvanic exchanges.[11-12] The yielded alloys generally maintain the original kernel skeletons, and only one or a few positions are exchanged, yielding single-site or multiple-site replacements.[13-22] For example, the silver atom located in the middle of the central Ag_{12} icosahedron of $[Ag_{25}(SR)_{18}]^-$ can be replaced by gold, to form $[AuAg_{24}(SR)_{18}]^-$, leading to a significant enhancement of photoluminescence.[13] Moreover, multiple-site replacements on the Ag_{12} icosahedron can also occur upon adding extra Au atoms to $[AuAg_{20}\{Se_2P(O^iPr)_2\}_{12}]^+$, forming $[Au_3Ag_{17}\{Se_2P(O^iPr)_2\}_{12}]^+$ accompanied with symmetry changes.[17] A similar idea was used to dope $Ag_{29}(SSR)_{12}(PPh_3)_4$ stepwise, first with copper to produce $Ag_{17}Cu_{12}(SSR)_{12}(PPh_3)_4$, and then with gold to reach the trimetallic alloy $AuAg_{16}Cu_{12}(SSR)_{12}(PPh_3)_4$ (SSR = benzene-1, 3-dithiolate).[23] The three isoelectronic NCs retain the same structural framework.

Thus, stepwise doping is a successful strategy to prepare trimetallic NCs.[20-21,23-24] Following the same strategy, we have isolated bimetallic and trimetallic M_{20} alloys, $[Cu_{3.5}Ag_{16.5}(dtp)_{12}]$ and $[Cu_{2.5}AuAg_{16.5}(dtp)_{12}]$ (dtp = $S_2P(O^nPr)_2$).[21] It is worth noting that, in the above described examples, the metal nuclearity and the number of ligands are maintained upon doping.[21,23] This can be possibly due to the innate bite angle of the dithiolate ligand, which provides less flexibility to the NC surface. In this context, increasing or decreasing the nuclearity of M_{20} NCs is restricted to a certain extent, which may explain the fact that only homoleptic silver-rich M_{20} or M_{21} NCs could be isolated so far.[16-18,20-21,25] Therefore, introducing hetero-donor ligands onto the cluster surface should be the key for allowing nuclearity modifications. In the broadly studied phosphine-protected Au NCs, the labile P-Au bond provides tremendous advantages in ligand exchange with other organic ligands such as thiolate ligands, encouraging the development of heteroleptic NCs.[26] In contrast to the relatively weak Au-P bonding, the strong Au-S bonding leads to the formation of highly stable Au NCs, making them difficult to undergo phosphine-ligand exchange reactions. A recent study reports the successful introduction of diphosphine ligands onto the cluster surface by adding Au-diphosphine complexes to a thiolate-protected Au NC, $[Au_{23}(SR)_{16}]^-$.[27] Motivated by this successful example, we adopted a similar strategy with Ag NCs. In this work, PPh_3 ligands have been introduced onto the NCs successfully together with the dopant. A bimetallic M_{17} NC, $[Au@Au_4Ag_{12}(dtp)_7(PPh_3)_4]^{2+}$ (**1**), and a trimetallic M_{16} NC, $[Pt@Au_4Ag_{11}(dtp)_7(PPh_3)_4]$ (**2**), have been isolated and characterized by X-ray crystallography, UV-Vis, and DFT calculations. Taking into account that Pt(0), Ag(0) and Au(0) are providing 0, 1 and 1 electron to the cluster count, respectively, and that the dtp ligands are formally anionic, both **1** and **2** are 8-electron NCs. To our knowledge, eight-

[a] *Department of Chemistry, National Dong Hwa University, Hualien 974301, Taiwan (Republic of China). E-mail: chenwei@gms.ndhu.edu.tw*
[b] *Univ Rennes, CNRS, ISCR-UMR 6226, F-35000 Rennes, France. E-mail: jean-yves.saillard@univ-rennes1.fr*

†Electronic Supplementary Information (ESI) available: [Experimental, ESI-MS, NMR spectra, and DFT calculations]. See DOI: 10.1039/x0xx00000x

electron M_{17}[28-31] and M_{16}[32-33] NCs were rarely reported compared to the large family of M_{25} 8-electron systems.

The syntheses of **1** and **2** (Scheme 1) were carried out by adding as-synthesized Au(PPh_3)Cl to $[M@Ag_{20}(dtp)_{12}]^z$ (M = Au, z = +1 for **1**; M = Pt, z = 0 for **2**), with the 4:1 molar ratio. Conceptually, when the additional Au proceeds to a galvanic reaction with the Ag_{12} core, the protective ligand shell is assumed to open a small window allowing the PPh_3 ligands to enter the surface shell, resulting in the partial removal of dtp ligands. Consistently, direct addition of PPh_3 ligands to $[M@Ag_{20}(dtp)_{12}]^z$ did not reveal any sign of PPh_3 coordination. It thus appears that additional ligands can coordinate to the metal core only after metal exchange.

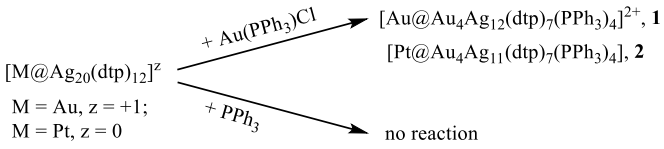

Scheme 1 Synthetic route of **1** and **2**.

The X-ray structures of **1** and **2** are anatomized in Fig. 1 and 2, respectively. Selected bond lengths are given in Table 1. The complete structure of the dication **1** (isolated as its hexafluorophosphate salt) is shown in Fig. 1a. The M_{17} metal framework approaches ideal C_2 symmetry (Fig. 1b) which can be seen as an Au-centered Au_4Ag_8 icosahedron with four additional silver atoms (Ag_{bri}). Surprisingly, *these outer Ag_{bri} atoms are all edge-bridging instead of being face-capping, as commonly observed in the homoleptic ligand-stabilized NCs*.[11,25]

The Ag_{bri}-Ag_{ico} separations (2.922(5)-3.074(4) Å, avg. 2.990(4) Å) show negligible differences with the M_{ico}-M_{ico} distances (2.838(3)-3.017(3) Å, avg. 2.910(3) Å). Four Au atoms are arranged on four consecutive vertices of the icosahedron, and each Au atom bears a terminal PPh_3 ligand (Fig. 1c) with an average P-Au distance of 2.310(9) Å. The arrangement of

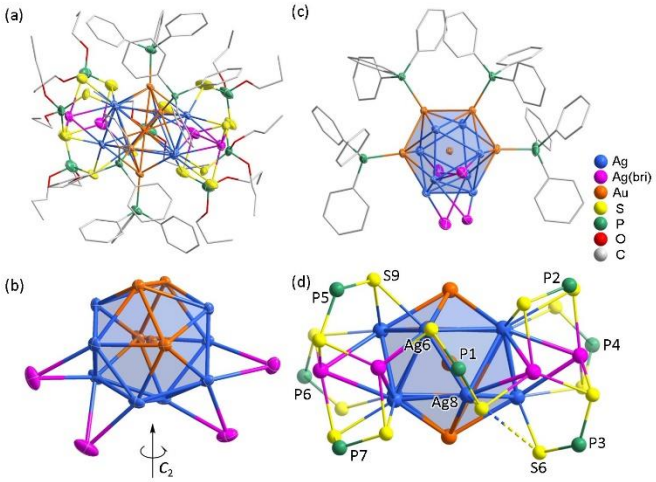

Fig. 1 (a) The total structure of $[Au@Au_4Ag_{12}\{S_2P(O^nPr)_2\}_7(PPh_3)_4]^{2+}$, **1**. (b) The Au_5Ag_{12} metal framework (Thermal ellipsoid were drawn at 30% probability). (c) With four PPh_3 (d) With seven dtp ligands without propoxy groups.

seven dtp ligands (Fig. 1d) matches approximately the presence of the *pseudo* C_2 axis which passes through the central Au atoms and the middle of Ag6-Ag8. However, the location of the dtc ligand related to P1 is slightly off this *pseudo* axis, leading to an Ag8…S6 distance (3.602 Å) larger than the Ag6-S9 one (2.741 Å), thus lowering the cluster symmetry to C_1. The coordination mode of the dtp ligands related to P1 and P5 is $\eta^4(\mu_2, \mu_2)$, that related to P2 an d P7 is $\eta^3(\mu_2, \mu_2)$ and that related to P3, P4 and P6 is $\eta^3(\mu_2, \mu_1)$.

The X-ray structure of the neutral compound **2** turned out to be a co-crystal composed of 75% $[PtAu_4Ag_{11}(dtp)_7(PPh_3)_4]$ (**2a**) and 25% $[PtAu_5Ag_{10}(dtp)_7(PPh_3)_4]$ (**2b**) with the fifth substituted Au atom disordered at two positions (Fig. S1). Thus, the following discussion focuses only on the major

Table 1 Selected experimental (X-ray) and DFT-computed data for **1** and **2**. Values into bracket are computed Wiberg bond indices. NAO = natural atomic orbital.

Distances (Å)	**1** (X-ray)	**1** (DFT)	**2** (X-ray)	**2a** (DFT)
M_{cent}-M_{ico}	2.7093(15)-2.854(3) avg. 2.768(2)	2.764-2.912 avg. 2.849 [0.131]	2.6946(5)-2.9094(9) avg. 2.7631(7)	2.774-2.975 Avg. 2.821 [0.153]
M_{ico}-M_{ico}	2.838(3)-3.017(3) avg. 2.910(3)	2.882-3.144 avg. 3.015 [0.063]	2.8106(5)-3.0558(8) avg. 2.9055(7)	2.854-3.126 avg. 2.965 [0.071]
M_{ico}-$M_{bri/cap}$	2.922(5)-3.074(4) avg. 2.990(4)	2.977-3.144 avg. 3.092 [0.028]	2.8291(8)-3.2649(10) avg. 3.0183(9)	2.896-3.518 avg. 3.082 [0.043]
P-Au	2.301(10)-2.331(7) avg. 2.310(9)	2.396-2.412 avg. 2.403 [0.358]	2.3066(19)-2.3225(19) avg. 2.315(2)	2.393-2.412 avg 2.403 [0.342]
S-Ag	2.387(10)-2.956(15) avg. 2.557(13)	2.484-3.691 avg. 2.680 [0.194]	2.422(2)-2.676(2) avg. 2.537(2)	2.486-2.735 avg. 2.582 [0.206]

NAO charges	**1** (DFT)	**2a** (DFT)
M_{cent}	-0.55	-1.10
avg. M_{ico}	0.02	0.06
avg. $Ag_{bri/cap}$	0.40	0.37

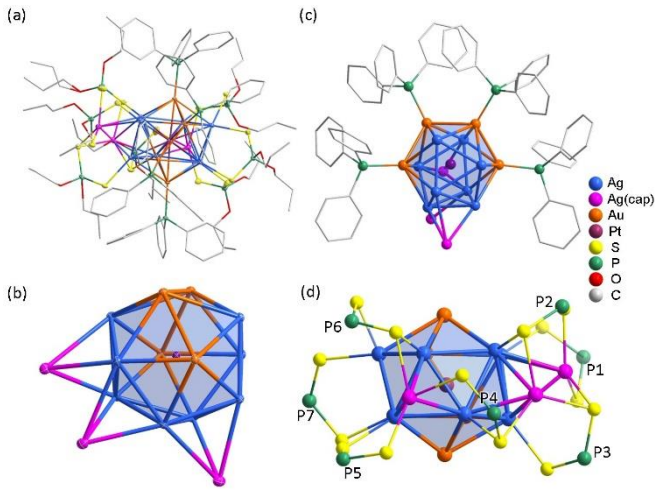

compound **2a**.

Fig. 2 (a) The total structure of $[Pt@Au_4Ag_{11}\{S_2P(O^nPr)_2\}_7(PPh_3)_4]$, **2**. (b) The $PtAu_4Ag_{11}$ metal framework (Thermal ellipsoid with 50% probability). (c) With the four PPh_3 ligands (d) With the seven dtp ligands (propoxy groups omitted).

Its complete structure is shown in Fig. 2a. The M_{16} metal framework can be seen as a Pt-centered Au_4Ag_8 icosahedron capped by three silver atoms (Ag_{cap}). The average M_{cent}-M_{ico} (2.7631(7) Å) and M_{ico}-M_{ico} distances (2.9055(7) Å) in **2a** are similar to **1**, indicating the two icosahedral skeletons are almost identical. Unlike the four edge-bridging silvers presented in **1**, there are only three face-capping silvers in **2a** (Fig. 2b) with an average Ag_{cap}-M_{ico} distance of 3.0183(9) Å. Although this does not affect the coordination mode of the four icosahedral Au atoms terminally bonded to PPh_3 ligands (average P-Au distance: 2.315(2) Å, Fig. 2c), it influences the orientation of the seven dtp ligands (Fig. 2d), which this time adopt $\eta^3(\mu_2, \mu_1)$ and $\eta^2(\mu_1, \mu_1)$ coordination mode for P2, P3, P4, P6 and P1, P5, P7, respectively. Therefore, both the M_{16} metal framework and the entire structure of **2** possess only C_1 symmetry.

From the perspective of the outer shell in **1** and **2**, the PPh_3 ligands coordinate radially to the icosahedron Au atoms, thus resulting in a linear P-Au-M_{cent} arrangement (the average angle is 176.4° in **1** and 176.8° in **2**). It is of note that in the bicapped icosahedral metal framework of $[MAu_6Ag_8(SAr^F)_6(PPh_3)_6]$ (M = Pd, Pt, Ar^F = 3,5-$(CF_3)_2C_6H_3$), the six Au atoms also occupy icosahedral vertices in an Au_6 chair conformation, each being linearly coordinated to a PPh_3 ligand.[34] Thus, it is anticipated that linearly coordinated terminal ligands, such as alkyne, monothiol, or N-heterocyclic carbene could be introduced as hetero ligands in the galvanic or anti-galvanic replacement processes. The doping gold atoms occupy M_{ico} instead of M_{cap} positions in **1** and **2**, which fully agrees with a previous DFT investigation on 8-electron $[MAg_{20}(dtp)_{12}]$ species.[35]

Since in **1** and **2** the four PPh_3 ligands orient in the same way, *i.e.* that minimizing steric hindrance (Fig. 1c and 2c), the difference between the two structures lies in the fact that, with one bridging atom more than in the latter, the outer shell of the former is more crowded, resulting in edge-bridging Ag_{bri} rather than face-bridging Ag_{cap} atoms in the latter. In addition, it is also noted that the different formal valence charges of the superatomic kernels, $[Au@Au_4Ag_8]^{5+}$ in **1** and $[Pt@Au_4Ag_8]^{4+}$ in **2**, may have implications in their interaction with the outer shell. These results demonstrate that the number of capping metal atoms and the charge of the kernel significantly affect the ligand coordination when the heteroligand participates in the protective shell.

The ESI-MS of **2** (Fig. S2) shows two distributions that contain the molecular ion peaks of $[PtAu_4Ag_{11}(dtp)_7(PPh_3)_4 + Ag^+]^+$ at *m/z* 4818.8408 (calc. *m/z* 4818.1578 for [**2a** + Ag^+]$^+$) and $[PtAu_5Ag_{10}(dtp)_7(PPh_3)_4 + AgPPh_3^+]^+$ at *m/z* 5170.2764 (calc. *m/z* 5170.3283 for [**2b** + $AgPPh_3^+$]$^+$). Intriguingly these two peaks correspond to the compositions determined in the co-crystal of **2a** and **2b**. The other molecular ion peaks are likely to be species resulting from the fragmentation of the gas-phase-instable NCs of **2**. The detailed assignment of each peak is given in Fig. S2.

The $^{31}P\{^1H\}$ NMR spectrum of **1** (Fig. S3) shows two resonances at around 102.5 and 37.2 ppm, associated with the dtp and PPh_3 ligands, respectively. In contrast, the $^{31}P\{^1H\}$ NMR spectrum of **2** reveals several chemical shifts from 103 to 109 ppm, attributable to the various chemical environments of dtp ligands in the less symmetrical structure **2**.

The UV-vis spectrum of **1** (Fig. 3a) shows a high-energy band at 263 nm corresponding to π→π* transitions (LLCT). The

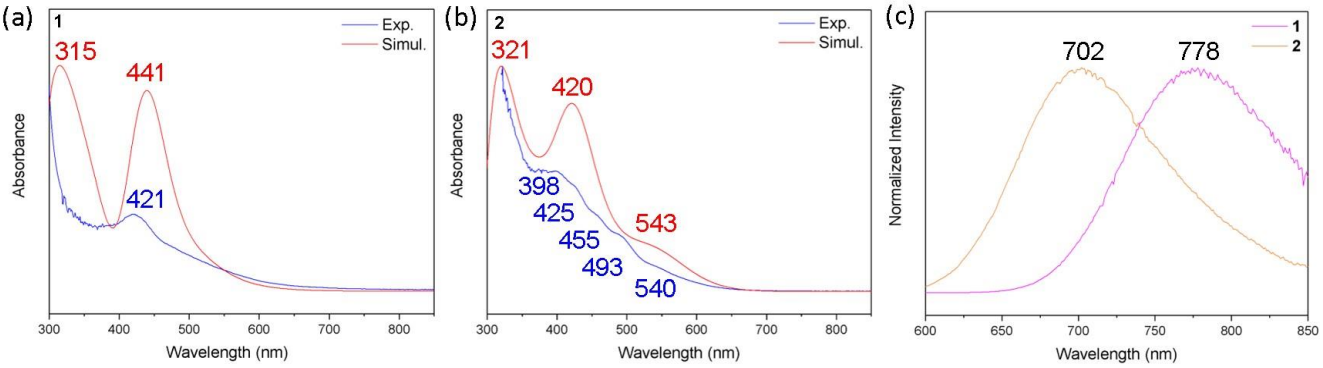

Fig. 3 (a) The absorption (blue) and simulated (red) spectra of **1**. (b) The absorption (blue) spectrum of **2** and the simulated (red) spectrum of **2a**. (c) The emission spectra of **1** (orange) and **2** (magenta) in 2-MeTHF glass at 77K.

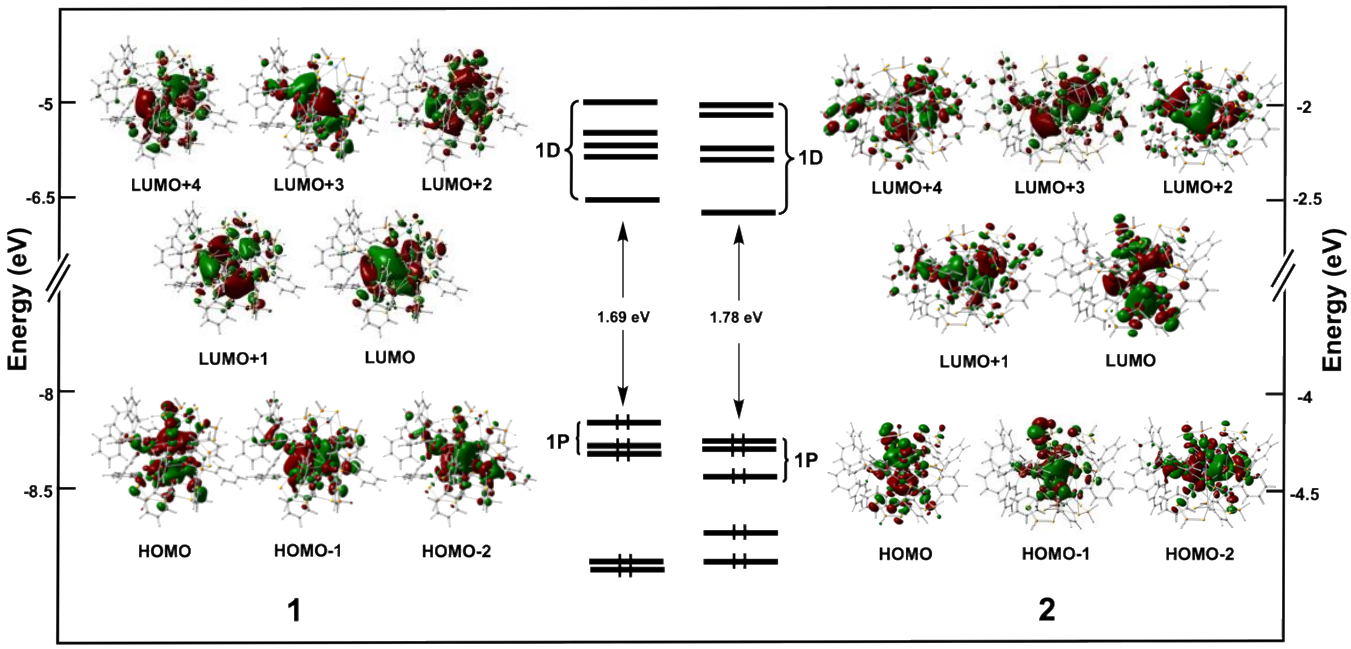

Fig. 4 Kohn-Sham frontier orbital diagrams of **1** and **2**. The low-lying 1S occupied orbitals are not shown.

low-energy absorption at 421 nm can be attributed to 1P →1D transitions (see below). The spectrum of **2** (Fig. 3b) displays five distinct absorption peaks at 398, 425, 455, 493, and 540 nm.

1 does not emit in solution at room temperature, but **2** reveals very weak emission at 725 nm. The glassy state of **1** and **2** at 77K shows red emission with maximal emission wavelengths of 778 and 702 nm, respectively (Fig. 3c). The lifetimes of **1** (Fig. S7) and **2** (Fig. S8) are 18 and 16 μs, respectively, characteristic of phosphorescence. For comparison, another example of an eight-electron alloy, $Au_4Ag_{13}(DPPM)_3(SR)_9$, displayed red emission at ~ 695 nm with a short-lived lifetime of 3.31 ns in the solution state.[31]

Density functional theory (DFT) calculations were carried out at the BP86/Def2SVP level (see Computational Details section in the supporting information) to shed some light on the bonding and properties of compounds **1** and **2a**, in which the $S_2P(O^iPr)_2$ ligands were replaced by S_2PH_2 in order to reduce computational cost. Selected computed date are given in Table 1. The optimized geometries of **1** and **2** are in good agreement with their X-ray counterparts. The M_{cent}-M_{ico} Wiberg bond index is typical for an 8-electron icosahedral system, whereas the M_{ico}-$M_{bri/cap}$ one is indicative of very weak covalent interaction, leaving the outer $M_{bri/cap}$ atoms as locally stable (nearly) planar tricoordinated 16-electron Ag(I) centers. The NAO charges of both NCs are similar, except for that of M_{cent}, as expected from to their different nature (Au *vs.* Pt). The Kohn-Sham MO diagrams of **1** and **2** are shown in Fig. 4. They exhibit rather large HOMO-LUMO gaps, in line with their stability. In both NCs, the three highest occupied orbitals can be identified as the 1P shell, whereas the five lowest vacant ones correspond to the 1D manifold, thus confirming their *superatomic* $1S^2\ 1P^6\ 1D^0$ configuration. TD-DFT calculations performed at the B3LYP/Def2SVP level on **1** and **2a** allow for simulating satisfyingly the shapes of their UV-vis spectra (Fig. 3a and 3b). In the case of **1**, the band at 441 nm is of 1P→1D *superatomic* nature (MMCT), whereas that at 315 nm corresponds to MLCT transitions. In the case of **2**, both bands a 543 and 420 nm are of 1P→1D nature, and that at 321 nm is of MLCT character.

Conclusions

In summary, a new synthetic pathway for introducing hetero ligands into dithiolate-protected nanoclusters was investigated. Owing to the high stability of dithiolate-protected nanoclusters, it is not easy to directly add other organic ligands, such as phosphine ligands, to achieve substitutions. The galvanic replacement triggered the phosphine addition when the parent $M@Ag_{20}$ NCs react with the Au-phosphine complex, yielding bimetallic M_{17} and trimetallic M_{16} NCs, $[Au@Au_4Ag_{12}(dtp)_7(PPh_3)_4]^{2+}$ and $[Pt@Au_4Ag_{11}(dtp)_7(PPh_3)_4]$. A prolonged reaction time in the same conditions does not yield a higher number of Au replacements. The results exhibit the modification of cluster surface, nuclearity, and also optical properties. The experimental absorption spectra are well-reproduced by TD-DFT calculations, where the low-energy bands at 441 nm (in **1**) and 420, 543 nm (in **2**) correspond to 1P→1D transitions. This method offers opportunities to design new heteroleptic NCs and maps out the possibility of NC surface engineering.

Conflicts of interest

There are no conflicts to declare.

Acknowledgements

This work was supported by the National Science and Technology Council (111-2123-M-259-002), and the GENCI computing resource (grant A0090807367). The authors gratefully acknowledge the Instrumentation Center of National Taiwan Normal University (NSTC 111-2731-M-003-001). HL thanks the China Scholarship Council for a Ph.D. grant.

References

1 C. M. Aikens, R. Jin, X. Roy and T. Tsukuda *J. Chem. Phys.*, 2022, **156**, 170401.
2 J. Yang, F. Yang, C. Zhang, X. He and R. Jin *ACS Materials Lett.*, 2022, **4**, 1279.
3 X. Kang, Y. Li, M. Zhu and R. Jin *Chem. Soc. Rev.*, 2020, **49**, 6443.
4 S. Takano and T. Tsukuda *J. Am. Chem. Soc.*, 2021, **143**, 1683.
5 T. Kawawaki, Y. Imai, D. Suzuki, S. Kato, I. Kobayashi, T. Suzuki, R. Kaneko, S. Hossain and Y. Negishi *Chem. Eur. J.*, 2020, **26**, 16150.
6 A. Ghosh, O. F. Mohammed and O. M. Bakr *Acc. Chem. Res.*, 2018, **51**, 3094.
7 I. Chakraborty and T. Pradeep *Chem. Rev.*, 2017, **117**, 8208.
8 T.-H. Chiu, J.-H. Liao, F. Gam, I. Chantrenne, S. Kahlal, J.-Y. Saillard and C. W. Liu *J. Am. Chem. Soc.*, 2019, **141**, 12957.
9 Y. Yang, T. Jia, Y.-Z. Han, Z.-A. Nan, S.-F. Yuan, F.-L. Yang and D. Sun *Angew. Chem. Int. Ed.*, 2019, **58**, 12280.
10 Z. Wang, R. Senanayake, C. M. Aikens, W.-M. Chen, C.-H. Tung and D. Sun *Nanoscale*, 2016, **8**, 18905.
11 S. Wang, Q. Li, X. Kang and M. Zhu *Acc. Chem. Res.*, 2018, **51**, 2784.
12 B.-L. Han, Z. Wang, R. K. Gupta, L. Feng, S. Wang, M. Kurmoo, Z.-Y. Gao, S. Schein, C.-H. Tung and D. Sun *ACS Nano*, 2021, **15**, 8733.
13 M. S. Bootharaju, C. P. Joshi, M. R. Parida, O. F. Mohammed and O. M. Bakr *Angew. Chem. Int. Ed*., 2016, **55**, 922.
14 X. Kang, S. Jin, L. Xiong, X. Wei, M. Zhou, C. Qin, Y. Pei, S. Wang and M. Zhu *Chem. Sci.*, 2020, **11**, 1691.
15 S. Yang, J. Chai, Y. Lv, T. Chen, S. Wang, H. Yu and M. Zhu *Chem. Commun.*, 2018, **54**, 12077.
16 W.-T. Chang, P.-Y. Lee, J.-H. Liao, S. Kahlal, K. K. Chakraharj, J.-Y. Saillard and C. W. Liu *Angew. Chem. Int. Ed.*, 2017, **56**, 10178.
17 W.-T. Chang, S. Sharma, J.-H. Liao, S. Kahlal, Y.-C. Liu, M.-H. Chiang, J.-Y. Saillard and C. W. Liu *Chem. Eur. J.*, 2018, **24**, 14352.
18 Y.-R. Lin, P. V. V. N. Kishore, J.-H. Liao, S. Kahlal, Y.-C. Liu, M.-H. Chiang, J.-Y. Saillard and C. W. Liu *Nanoscale*, 2018, **10**, 6855.
19 F. Gam, I. Chantrenne, S. Kahlal, T.-H. Chiu, J.-H. Liao, C. W. Liu and J.-Y. Saillard *Nanoscale*, 2022, **14**, 196.
20 Y.-J. Zhong, J.-H. Liao, T.-H. Chiu, F. Gam, S. Kahlal, J.-Y. Saillard and C. W. Liu *J. Chem. Phys.*, 2021, **155**, 034304.
21 W.-J. Yen, J.-H. Liao, T.-H. Chiu, Y.-S. Wen and C. W. Liu *Inorg. Chem.*, 2022, **61**, 6695.
22 M. Kim, K. L. D. M. Weerawardene, W. Choi, S. M. Han, J. Paik, Y. Kim, M.-G. Choi, C. M. Aikens and D. Lee *Chem. Mater.*, 2020, **32**, 10216.
23 X. Kang, H. Abroshan, S. Wang and M. Zhu *Inorg. Chem.*, 2019, **58**, 11000.
24 T. G. M. M. Kappen, P. P. J. Schlebos, J. J. Bour, W. P. Bosman, J. M. M. Smits, P. T. Beurskens and J. J. Steggerda *Inorg. Chem.*, 1994, **33**, 754.
25 S. Sharma, K. K. Chakrahari, J.-Y. Saillard and C. W. Liu *Acc. Chem. Res.*, 2018, **51**, 2475.
26 R. H. Adnan, J. M. L. Madridejos, A. S. Alotabi, G. F. Metha and G. G. Andersson *Adv. Sci.*, 2022, **9**, 2105692.
27 Q. Li, S. Yang, J. Chai, H. Zhang and M. Zhu *Nanoscale*, 2022, **14**, 15804.
28 H. Yang, Y. Wang, J. Lei, L. Shi, X. Wu, V. Mäkinen, S. Lin, Z. Tang, J. He, H. Häkkinen, L. Zheng and N. Zheng *J. Am. Chem. Soc.*, 2013, **135**, 9568.
29 C. Zhou, H. Li, F. Ke, C. Zhu, P. Pan, W. W. Zu, X. Kang, Y. Song and M. Zhu *J. Chem. Phys.*, 2021, **154**, 184302.
30 Y. Song, Y. Lv, M. Zhou, T.-Y. Luo, S. Zhao, N. L. Rosi, H. Yu, M. Zhu and R. Jin *Nanoscale*, 2018, **10**, 12093.
31 T. Chen, S. Yang, J. Chai, Y. Song, J. Fan, B. Rao, H. Sheng, H. Yu and M. Zhu *Sci. Adv.*, 2017, **3**, e1700956.
32 Z.-R. Wen, Z.-J. Guan, Y. Zhang, Y.-M. Lin and Q.-M. Wang *Chem. Commun.*, 2019, **55**, 12992.
33 M. Zhou, C. Qi, X. Yan, X. Li, S. Jin and M. Zhu *Chem. Eur. J.*, 2021, **27**, 17554.
34 S. Takano and T. Tsukuda *Chem. Lett.*, 2021, **50**, 1419.
35 F. Gam, I. Chantrenne, S. Kahlal, T.-H. Chiu, J.-H. Liao, C. W. Liu and J.-Y. Saillard *Nanoscale*, 2021, **14**, 196.